Int. J. Heat Mass Transfer. Vol. 34, No. 1, pp. 181–197, 1991
Printed in Great Britain

0017–9310/91 $3.00 + 0.00

The mathematical modelling and computer simulation of fire development in aircraft

E. R. GALEA
Centre for Numerical Modelling and Process Analysis, Thames Polytechnic, Wellington Street, London SE18 6PF, U.K.

and

N. C. MARKATOS
Department of Chemical Engineering, National Technical University, 106 82 Athens, Greece

(*Received* 2 *November* 1988 *and in final form* 13 *March* 1990)

Abstract—The paper presents a steady-state or transient, three-dimensional mathematical field model describing aircraft cabin fires. The fire is modelled by a simple heat source, and the simulation is intended to represent non-spreading fires. The computer code implementing the model uses a body-fitted coordinate (BFC) formulation to describe accurately the interior of the aircraft, that is neither Cartesian nor polar–cylindrical. The model is first used to predict the experimental results obtained from a series of fire tests performed in a Boeing-737 fuselage (without fittings). Both steady-state and transient results are presented and discussed. Then the effect of openings in the fuselage and cabin compartmentation on the temperature distribution within the empty aircraft cabin is investigated. With the forward and aft bulkhead doors open, allowing for natural convection, the temperatures are kept to tolerable levels. When the forward door is closed while the aft is kept open, temperatures increase throughout the cabin even in the aft section. With both forward and aft doors open, the cabin is partitioned into two communicating sections, the forward section containing the fire. When compared to the non-compartmented case temperatures in the aft section decrease while temperatures in the forward section increase. With the cabin fitted with seats, ceiling panels and overhead stowage bins the effect of the aircraft's air-conditioning system on the temperature distribution within the burning fuselage is examined. The results suggest that a reverse flow situation (i.e. cold air injected through floor vents and hot air sucked out at ceiling vents) greatly reduces the temperature throughout the fuselage. It is concluded that, although insufficiently validated as yet due to the lack of extensive and suitable experimental data, the model is promising.

1. INTRODUCTION

AIRCRAFT accidents are often accompanied by fire. The large quantities of flammable fuel carried by modern aircraft (214 000 and 105 000 l for the B-747 and L-1011, respectively) and the cabin design, which consists of a densely populated enclosure lined and furnished with organic (largely synthetic) materials (4200 kg of such material is carried on a B-747) makes the possibility of fire a major concern.

Life threatening aircraft cabin fires belong to one of two groups, the so-called post-crash fire and the in-flight fire. The post-crash fire involves survivable crashes, i.e. incidents in which occupants survive the initial trauma of impact. In post-crash fires the fire is initiated outside the cabin usually due to a fuel spill. The fire then attacks the aircraft cabin gaining entry via breaks due to impact damage. A Boeing study of more than 150 survivable crashes suggests that about 1300 people who may have survived the impacts perished as a result of fire [1]. In-flight fires mostly occur in accessible areas such as a galley or toilet. In the 20 years from 1964 to 1984 approximately 300 cases of in-flight fires have been reported, of these some 52 have proved fatal, accounting for about 1000 deaths [1–3].

To uncover details concerning the fire-dynamics involved and the hazards responsible for preventing escape by passengers and ultimately their death, it is necessary to perform simulations of several possible fire scenarios. The simulation may be either numerical, i.e. computer-based mathematical model or experimental fire tests.

Mathematical modelling offers a cheaper and more general alternative to the experimental approach, provided that the models can be reliably validated. Both zone and field models have been implemented in describing aircraft cabin fires [3, 4]. Zone modelling represents the state-of-the-art approach currently in use; DACFIR (e.g. ref. [5]; for a comprehensive list see ref. [3]) being the most sophisticated of the zone modelling packages available for aircraft fires. The field modelling formulation, while still in its infancy, is emerging as the 'new technology' for modelling of aircraft cabin fires. It is already becoming a more widely accepted tool within the building fire community [6–12]. Previous attempts at modelling aircraft cabin fires using the field modelling approach have

NOMENCLATURE

$\mathbf{e}^j$	covariant base vectors
$\mathbf{e}_i$	contravariant base vectors
$\mathbf{F}$	general force vector
$\mathbf{g}_n$	non-orthogonal unit vectors
$\mathbf{i}_j$	Cartesian unit vectors ($j = 1, 2, 3$)
k	turbulent kinetic energy
$\mathbf{n}$	outward drawn normal vector
P	pressure
$\mathbf{R}$	radial position vector
S_φ	source terms
u_j	velocity components
$\mathbf{V}$	velocity vector
x_j	Cartesian coordinates.

Greek symbols

Γ	exchange coefficient
δ_j^i	Kronecker delta
ε	dissipation rate of k
μ	viscosity
μ_l	laminar viscosity
ξ_n	curvilinear coordinates
ρ	density
σ	Prandtl number
$\bar{\bar{\tau}}$	stress tensor
φ_n	scalar variable
$\boldsymbol{\omega}$	angular velocity vector.

Other symbol

∇	vector differential operator.

been confined to two-dimensional studies (e.g. ref. [13]; for a comprehensive list see ref. [3]). Satoh and Kurvishi [14] have performed a three-dimensional simulation of an aircraft cabin fire, but this study lacked an accurate description of the aircraft cabin geometry. More recently Galea and Markatos [15–17] have modelled aircraft fires using non-orthogonal, curvilinear, body-fitted coordinates (BFCs). This approach allows realistically shaped aircraft cabins to be simulated (see Fig. 1).

In the following sections a mathematical field model describing the in-flight fire scenario is presented and discussed. The model, still under development, attempts to simulate turbulent, buoyant fluid flow and heat transfer within a realistically shaped aircraft cabin. The dimensions of the cabin are that of a Boeing-737; its length is 17.1 m with a width of 3.3 m at the floor and a maximum height of 2.1 m. The volume is 104 m^3. Doors of dimensions 1.5 m × 0.9 m are situated in the forward and aft bulkheads [18] (see Fig. 1). The ambient temperature was 29°C. Both steady-state and time-dependent simulations are presented here.

In an attempt to validate the numerical model, calculated results are compared with a set of experimental data from cabin fire tests conducted at the

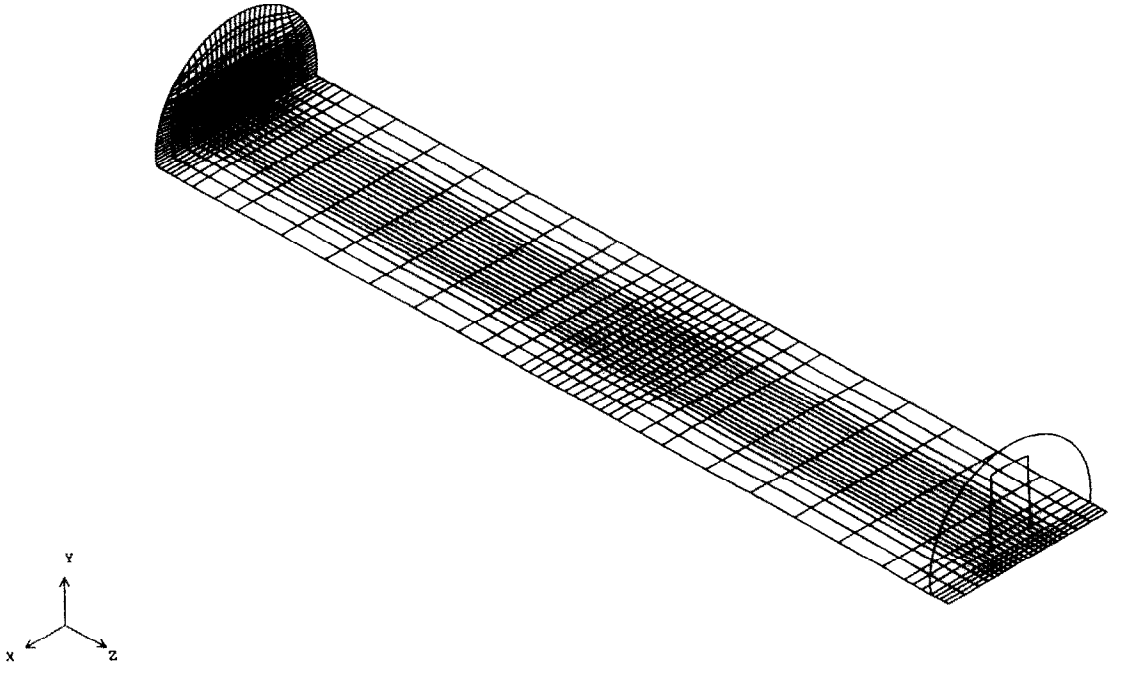

FIG. 1. Body fitted coordinate grid used in numerical simulations.

Johnson Space Centre [18]. These tests consisted of a series of 25 experiments conducted in the above fuselage. Test 6 was chosen as the most appropriate for comparison purposes. In this test the fire source, a fuel pan of dimensions 0.61 m × 0.61 m containing 4.5 l of Jet A-1 fuel, was located on the floor just off centre. Over the first 6 min of the burn this corresponded to a constant heat release rate of 239 kW. During the last 4 min the heat release rate had dropped to a constant 50.7 kW. In test 6, the forward and aft bulkhead doors were left open allowing for natural ventilation.

Four sets of results are presented and discussed. The first group consists of a series of steady-state grid refinement/validation results, simulating the near equilibrium conditions which develop after 10 min of the burn. The fire is simulated by a volumetric heat source of 50.7 kW. The second group consists of a series of time-dependent simulations covering the first 4 min of the burn. The fire is simulated by a 239 kW volumetric heat source. The third set examines the effects of various cabin openings and compartmentation on the temperature distribution within the burning cabin. The fire, located on the floor, just off the cabin centre, is simulated again by a heat source of 50.7 kW. The fourth set represents a fire situation similar to that in the first group with the additional features of the cabin environmental control system and internal fittings included. The environmental control system consists of uniform venting at the ceiling and floor. The ceiling vents are situated at the top of the ceiling while the floor vents are located in the left and right corners where the side panels meet the floor. Both the ceiling and floor vents extend along the entire length of the cabin. From these vents either hot air may be sucked out of, or cool air injected into the cabin. The venting rate is such that a complete air change is produced in 3 min. The fittings consist of two rows of seats and a ceiling unit including the passenger stowage bins. The seating configuration consists of a row of three seats abreast and a row of two seats abreast separated by an aisle. Seating in the vicinity of the heat source is not included (see Figs. 2(a) and (b)). While the dimensions of the cabin are modelled on the B-737 it has been necessary to approximate the furniture specifications.

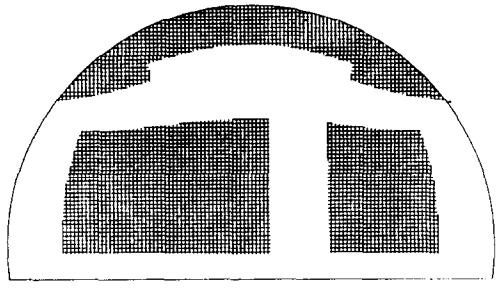

(a)

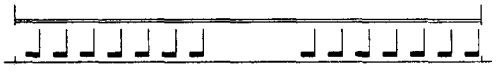

(b)

FIG. 2. (a) Cylindrical section of aircraft cabin showing position of seats, ceiling panel and overhead stowage bins. (b) Longitudinal section of cabin showing position of seats and ceiling panel and the open forward and aft doorway.

2. THE MATHEMATICAL FORMULATION

The starting point of the analysis is the set of three-dimensional, partial differential equations that govern the phenomena of interest here. This set consists, in general, of the following equations: the continuity equation; the three momentum equations that govern the conservation of momentum per unit mass (e.g. velocity) in each of the three space directions (the Navier–Stokes equations); the equations for conservation of energy and species concentrations; and, the equations for a turbulence model (in this case the k–ε model). The computer code PHOENICS [19] is used to solve this set of equations.

2.1. *The momentum equations*

The momentum equations in general non-orthogonal coordinate systems are derived from the following general, coordinate-free, vector form of the Navier–Stokes equations:

$$\rho\left[\frac{\partial \mathbf{V}}{\partial t}+(\mathbf{V}\cdot\nabla)\mathbf{V}\right]-\nabla\cdot\bar{\bar{\tau}}=-\nabla p+\mathbf{F} \qquad (1)$$

where $\mathbf{V}$ is the velocity vector, ∇ the vector differential operator, $\mathbf{F}$ a general force vector, and $\bar{\bar{\tau}}$ the stress tensor, which represents both viscous stresses and Reynolds stresses arising from the ensemble averaging of the unsteady momentum equations in turbulent flows.

Certain velocity vector and derivative relations are defined here and will be used later. Let X_j be Cartesian coordinates with unit vectors $\mathbf{i}_j$. Then the velocity vector $\mathbf{V}$ is

$$\mathbf{V}=\sum_{j=1}^{3}u_j\mathbf{i}_j=u_1\mathbf{i}_1+u_2\mathbf{i}_2+u_3\mathbf{i}_3=u_1\mathbf{i}+u_2\mathbf{j}+u_3\mathbf{k} \qquad (2)$$

where u_j are the velocity components.

In this system we also have

$$\nabla=\sum_{j=1}^{3}\mathbf{i}_j\frac{\partial}{\partial x_j} \qquad (3)$$

and

$$\nabla\cdot\bar{\bar{\tau}}=(\nabla\cdot\mu\nabla)\mathbf{V}+\sum_{\lambda=1}^{3}\left[\sum_{j=1}^{3}\frac{\partial}{\partial x_j}\left(\mu\frac{\partial u_j}{\partial x_\lambda}\right)\right]\mathbf{i}_\lambda \qquad (4)$$

where the second term is zero for incompressible flows with constant viscosity μ.

The force **F** includes such contributions as the centrifugal force $-\rho\omega\times\omega\times R$ and the Coriolis force term $-2\rho\omega\times\mathbf{V}$, where ω is the angular velocity vector equal to $\omega\mathbf{i}_3$ and **R** is the radial position vector equal to

$$\mathbf{R} = R\cos\theta\,\mathbf{i} + R\sin\theta\,\mathbf{i},$$

where R is the radial coordinate.

When one considers BFCs there is a choice of either curvilinear orthogonal or curvilinear non-orthogonal systems. The advantage of the former is that the transport equations are little different to their Cartesian counterparts, and their discretized forms possess nearly the same general form as for regular coordinate systems [20]. By contrast the equations in general non-orthogonal coordinates and their discretized versions are considerably more complicated, and may give rise to computational problems [21]. The orthogonal coordinates present however several disadvantages. The coordinate mesh must be generated by some means, such as usually the solution of differential equations expressing the family of curves orthogonal to a chosen family of curves that fits the domain. This process can be very costly (the setting of the grid can be as expensive as the solving of the equations [22]). Furthermore, orthogonal lines so generated often distribute themselves in an inconvenient and inefficient manner (particularly in regions with non-orthogonally intersecting boundaries) and restrict the flexibility of selective grid refinement for a given shape. Non-orthogonal coordinates are more versatile: the mesh is easier to generate and distribute, and can be aligned with streamlines, thus suppressing 'false-diffusion' [21, 23]. Although the code used, PHOENICS, caters for both systems easily, the non-orthogonal option was selected for this work and is described below.

Let us consider a general non-orthogonal system defined as

$$\xi_n = \xi_n(X_1, X_2, X_3), \quad n = 1, 2, 3 \tag{5}$$

where ξ_n are the curvilinear coordinates at any point, and X_1, X_2, X_3 are its Cartesian coordinates. Let $\mathbf{g}_n$ be the non-orthogonal unit vectors along the three coordinate directions. Various options of formulating the momentum equation in the coordinate direction i arise by identifying $\mathbf{g}_n$ with some direction. Thus, by identifying $\mathbf{g}_n$ with the direction normal to the coordinate surface through which i passes (in other words, by identifying $\mathbf{g}_n$ with the covariant base vector $\mathbf{e}^i$) we can derive the equation for the *component* of momentum in the coordinate direction i (see Fig. 3(a)), for

$$\mathbf{e}^i\cdot\mathbf{V} = \mathbf{e}^i\cdot(v^j\mathbf{e}_j) = v^i. \tag{6}$$

The covariant vectors are defined in terms of the contravariant vectors thus

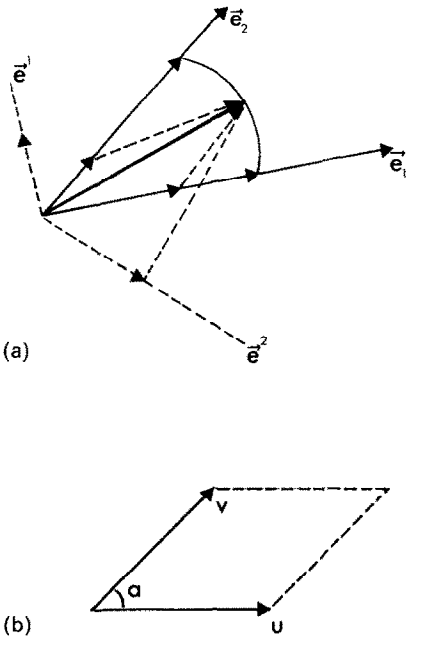

FIG. 3. Definition of vector resolutes and components.

$$\mathbf{e}^1 = \mathbf{e}_2\times\mathbf{e}_3/[\mathbf{e}_1\cdot\mathbf{e}_2\times\mathbf{e}_3],$$
$$\mathbf{e}^2 = \mathbf{e}_3\times\mathbf{e}_1/[\mathbf{e}_1\cdot\mathbf{e}_2\times\mathbf{e}_3], \text{ etc.} \tag{7}$$

Consider the simple oblique Cartesian system of Fig. 3(b), where the u velocity is aligned with the x-direction. The contravariant vectors may be written directly in terms of the Cartesian vectors **i**, **j**, **k**

$$\mathbf{e}_1 = \mathbf{i}, \mathbf{e}_2 = \cos\alpha\mathbf{i} + \sin\alpha\mathbf{j}, \mathbf{e}_3 = \mathbf{k}$$

and

$$\mathbf{e}_1\cdot\mathbf{e}_2\times\mathbf{e}_3 = \sin\alpha, \mathbf{e}_3\times\mathbf{e}_1 = \mathbf{k}\times\mathbf{i} = \mathbf{j}$$

and therefore

$$\mathbf{e}^1 = (-\cos\alpha\mathbf{j} + \sin\alpha\mathbf{i})/\sin\alpha, \mathbf{e}^2 = \mathbf{j}/\sin\alpha.$$

Recall that the definition of the base vectors $\mathbf{e}^i$ is such as to ensure the orthogonality condition

$$\mathbf{e}^i\cdot\mathbf{e}_j = \delta^i_j \text{ (Kronecker)}$$

and that of course $\mathbf{e}^1\cdot\mathbf{e}^1$ is not unity since these are not unit vectors, as seen from their definitions.

It is obvious from the above that in general non-orthogonal coordinates there exists a number of options in formulating the transport equations [21]. They arise from the many degrees of freedom available in the choice of velocity components and their alignment or otherwise with the coordinates, as well as the direction of resolution of the momentum equation. The main options have been presented and analysed in refs. [21, 24] and are: whether the velocity directions are spatially invariant or not (leading to strong or weak conservation forms); whether the velocity components are in the direction of or normal to

the coordinate directions; whether physical or non-physical velocities are used (leading to covariant or contravariant forms, respectively); and whether the momentum equation is resolved into components aligned with or normal to the coordinate directions. All these are naturally equivalent to each other from the physical point of view, but present substantial differences from the numerical analysis point of view. The most extensively used option is the form with vectors and tensors resolved into their Cartesian components.

More recent work using contravariant physical velocity components is reported in ref. [21].

The procedure embodied in PHOENICS uses the equation for the *resolute* of the momentum along the coordinate direction i. This is obtained by identifying $\mathbf{g}_n$ with the unit vector tangent to direction n, and forming the vector dot product of $\mathbf{g}_n$ with equation (1). The momentum equation is solved in terms of the resolutes (e.g. the projections) of the velocity vector $\mathbf{V}$ into the local coordinate directions, e.g. the resolutes are defined as [25]

$$V_n = \mathbf{g}_n \cdot \mathbf{V} = \sum_{j=1}^{3} g_{n,j} U_j, \quad n = 1,2,3 \tag{8}$$

where U_j are the Cartesian components and the unit tangent vectors in the three coordinate directions are

$$\mathbf{g}_n = \mathbf{X}_{,\xi_n} / |\mathbf{X}_{,\xi_n}| = \sum_{j=1}^{3} g_{n,j} \mathbf{i}_j, \quad n = 1,2,3 \tag{9}$$

with $\mathbf{X}$ being the position vector of a point, and the subscript $,\xi_n$ denotes a partial derivative with respect to the curvilinear coordinate ξ_n. To obtain the resolute of the momentum equation in each of the coordinate directions we form the dot product of unit tangent vectors with the momentum equation (1).

Thus

$$\mathbf{g}_n \cdot \left(\rho \frac{\partial \mathbf{V}}{\partial t}\right) + \mathbf{g}_n \cdot (\rho \mathbf{V} \cdot \nabla)\mathbf{V} - \mathbf{g}_n \cdot (\nabla \cdot \mu \nabla)\mathbf{V} - \mathbf{g}_n \cdot \mathbf{S}_\mu = -\mathbf{g}_n \cdot \nabla p - \mathbf{g}_n \cdot \mathbf{F} \tag{10}$$

where $\mathbf{S}_\mu$ represents the second term of equation (4).

We have from vector calculus

$$\nabla(\mathbf{g}_n \cdot \rho \mathbf{V}) = (\rho \mathbf{V} \cdot \nabla)\mathbf{g}_n + (\mathbf{g}_n \cdot \nabla)\rho \mathbf{V} + \rho \mathbf{V} \times (\nabla \times \mathbf{g}_n) + \mathbf{g}_n \times (\nabla \times \rho \mathbf{V}). \tag{11}$$

† Use is made of

$$\mathbf{V} \cdot \mathbf{g}_n \times (\nabla \times \mathbf{V}) = -\mathbf{g}_n \cdot (\mathbf{V} \times (\nabla \times \mathbf{V}))\mathbf{V} \tag{1}$$

$$(\mathbf{V} \cdot \nabla)\mathbf{V} = \nabla\left(\frac{|V_n|^2}{2}\right) - \mathbf{V} \times (\nabla \times \mathbf{V}) \tag{2}$$

$$\mathbf{V} \cdot \mathbf{V} \times (\nabla \times \mathbf{g}_n) = (\mathbf{V} \times \mathbf{V}) \cdot (\nabla \times \mathbf{g}_n) = 0 \text{ (since } \mathbf{V} \times \mathbf{V} = 0). \tag{3}$$

Thus

$$\mathbf{g}_n \cdot \nabla\left(\frac{|V_n|^2}{2}\right) = \mathbf{V} \cdot (\mathbf{g}_n \cdot \nabla)\mathbf{V}.$$

Taking the dot product of equation (11) with $\mathbf{V}$† we have

$$(\rho \mathbf{V} \cdot \nabla) V_n = \mathbf{V} \cdot (\rho \mathbf{V} \cdot \nabla)\mathbf{g}_n + \mathbf{g}_n \cdot (\rho \mathbf{V} \cdot \nabla)\mathbf{V}. \tag{12}$$

We also have for a scalar variable φ_n

$$\nabla \cdot (\rho \mathbf{V} \varphi_n) = \rho \mathbf{V} \cdot \nabla \varphi_n \tag{13}$$

and

$$(\nabla \cdot \mu \nabla)\mathbf{V} \cdot \mathbf{g}_n = \mathbf{g}_n \cdot (\nabla \cdot \mu \nabla)\mathbf{V} + \mathbf{V} \cdot (\nabla \cdot \mu \nabla)\mathbf{g}_n. \tag{14}$$

Using equations (12)–(14) we can write equation (10) as follows:

$$\mathbf{g}_n \cdot \left(\rho \frac{\partial \mathbf{V}}{\partial t}\right) + \nabla \cdot (\rho \mathbf{V} V_n) - (\nabla \cdot \mu \nabla) V_n - \mathbf{g}_n \cdot \mathbf{S}_\mu = -\mathbf{g}_n \cdot \nabla p + \mathbf{V} \cdot (\rho \mathbf{V} \cdot \nabla)\mathbf{g}_n - \mathbf{V} \cdot (\nabla \cdot \mu \nabla)\mathbf{g}_n - \mathbf{g}_n \cdot \mathbf{F} \tag{15}$$

and

$$(\mathbf{V} \cdot \nabla) V_n = \mathbf{V} \cdot (\mathbf{V} \cdot \nabla)\mathbf{g}_n + \mathbf{g}_n \cdot (\mathbf{V} \cdot \nabla)\mathbf{V}.$$

This is the general momentum equation for appropriate $\mathbf{F}$ forces (for example, the centrifugal force term $\mathbf{g}_n \cdot (\rho \omega \times \omega \times \mathbf{R})$ and the Coriolis force $\mathbf{g}_n \cdot (2\rho\omega \times \mathbf{V})$). The following derivate and velocity vector relationships are used to evaluate the various terms in equation (15).

From equations (3) and (9), the partial derivative in the direction ξ_n is

$$\frac{\partial}{\partial \xi_n} = \mathbf{g}_n \cdot \nabla = \sum_{j=1}^{3} g_{n,j} \frac{\partial}{\partial x_j} \tag{16}$$

with inverse

$$\frac{\partial}{\partial x_n} = \sum_{j=1}^{3} G_{n,j} \frac{\partial}{\partial \xi_j} \tag{17}$$

where $G_{n,j}$ the elements of the inverse matrix of the elements $g_{n,j}$ (see below).

2.2. *The continuity equation*

The continuity equation is solved in terms of the velocity *components* along the coordinate directions. These components, say, u_n,

$$\left[\mathbf{V} = \sum_{n=1}^{3} \mathbf{g}_n u_n\right]$$

are calculated from the velocity resolutes by solving the simultaneous equations

$$V_n = \sum_{j=1}^{3} \mathbf{g}_n \cdot (\mathbf{g}_j u_j), \quad n = 1,2,3. \tag{18}$$

The solution for the components in terms of the resolutes is

$$u_n = \sum_{j=1}^{3} G_{n,j} V_j, \quad n = 1,2,3 \tag{19}$$

where

$$G_{n,j}/\sigma = \begin{bmatrix} (1-c^2) & (bc-a) & (ac-b) \\ (bc-a) & (1-b^2) & (ab-c) \\ (ac-b) & (ab-c) & (1-a^2) \end{bmatrix} \tag{20}$$

where

$$a = \mathbf{g}_1 \cdot \mathbf{g}_2,\ b = \mathbf{g}_1 \cdot \mathbf{g}_3,\ c = \mathbf{g}_2 \cdot \mathbf{g}_3 \tag{21}$$

and the scalar coefficient σ is defined by

$$\sigma = [1-(a^2+b^2+c^2-2abc)]^{-1}. \tag{22}$$

For orthogonal coordinates, $a = b = c = 0$ and therefore $u_n = V_j$.

Using equations (2) and (19) it follows that

$$\mathbf{V} = \sum_{n=1}^{3} \mathbf{i}_n \sum_{j=1}^{3} G_{n,j} V_j = \sum_{j=1}^{3} \mathbf{Q}_j V_j \tag{23}$$

where the vectors $\mathbf{Q}_j$ for expanding $\mathbf{V}$ in terms of resolutes is

$$\mathbf{Q}_j = \sum_{n=1}^{3} G_{n,j} \mathbf{i}_n. \tag{24}$$

From equations (3), (17) and (21) we get for the vector differential operator

$$\nabla = \sum_{j=1}^{3} \mathbf{Q}_j \frac{\partial}{\partial \xi_j}. \tag{25}$$

A method for determining the gradient transformation vectors $\mathbf{Q}_j$ for general coordinates has been developed independently by Swanson [23] and by Parameswaran [26].

With these expressions we can evaluate all terms in equation (15), e.g. force, viscous and acceleration terms, and also solve the continuity equation. The curvilinear acceleration terms arise from the vector product $\mathbf{V} \cdot (\rho \mathbf{V} \cdot \nabla)\mathbf{g}_n$; and there are, in general, nine possible acceleration terms for each momentum equation (although they reduce to six due to the symmetry of the tensor). In cylindrical coordinates they reduce to the familiar centripetal and Coriolis terms. Some further details on the evaluation of these terms may be found in refs. [23, 26].

2.3. *The general φ-equation*

Equation (15) can be generalized [23] to provide the appropriate equation for any scalar variable

$$\nabla \cdot \mathbf{Q} = S\varphi_n \tag{26}$$

where

$$\mathbf{Q} = \rho \mathbf{V} \varphi_n - \Gamma_{\varphi_n} \nabla \varphi_n \tag{27}$$

and φ_n a general scalar variable, such as V_n, k, ε, etc.

For k, ε

$$S_k = G - \rho\varepsilon + G_B,\ S_\varepsilon = C_1 \varepsilon/k G - C_2 \rho \varepsilon^2/k \tag{28}$$

where in Cartesian-tensor form

$$G = \mu(\partial u_j/\partial x_i + \partial u_i/\partial x_j)\partial u_j/\partial x_i \tag{29}$$

where u_i, u_j the velocity components in the direction of the Cartesian coordinates x_i and x_j with $i = 1, 2, 3$, $j = 1, 2, 3$. The effective exchange coefficients for v_n, k, ε are

$$\Gamma_{v_n} = \mu_l + \mu_t = \mu, \quad \mu_t = \rho C_\mu \frac{k^2}{\varepsilon}$$

$$\Gamma_k = \mu_l + \mu_t/\sigma_{k,t}, \quad \Gamma_\varepsilon = \mu_l + \mu_t/\sigma_{\varepsilon,t} \tag{30}$$

where μ_l is the laminar viscosity, C_1, C_2, C_μ are turbulence model constants; and $\sigma_{k,t}$, $\sigma_{\varepsilon,t}$ are the turbulence Prandtl numbers for k and ε.

Buoyancy–turbulence interactions are not straightforward to predict; and lead also to difficulties in convergence of the numerical schemes. These interactions are accounted for in the generation term of the k-equation, equation (28) above, by the addition of the following term:

$$G_B = -B g \frac{\mu_t}{\sigma_{t,\omega}} \frac{\partial \varphi}{\partial y}$$

where B is the volume expansion coefficient. In stable stratification, G_B becomes a sink term so that the turbulent mixing is reduced. In unstable stratification, the buoyancy will enhance turbulence since G_B is positive. This treatment is based on the original work in refs. [27, 28], as modified in refs. [7, 29]. The buoyancy term appearing tentatively in the ε-equation in other k–ε calculations for buoyant flows [27, 28], has been omitted. There is no obvious physical reason for including such a term, and other related work indicated that it is completely insignificant [7]. More details may be found in refs. [7, 27, 28].

2.4. *Finite volume equations*

The finite volume equations can be derived in the same way as for regular grids, namely by applying integration of the equations over a control volume. Thus

$$\int_{\Delta V} \nabla \cdot \mathbf{Q}\, \mathrm{d}V = \int_S \mathbf{n} \cdot \mathbf{Q}\, \mathrm{d}S = \int_S \mathbf{n} \cdot (\rho \mathbf{V} \varphi_\eta - \Gamma_{\varphi_\eta} \nabla \varphi_\eta)\, \mathrm{d}S \tag{31}$$

where $\mathbf{n}$ is the outward drawn normal to any of the six surfaces defining ΔV and S denotes surface area. Integration entails assumptions about the distribution of the variables between nodes centred in each control volume. For the convection terms, all fluid properties are assumed uniform over cell faces; and, except in respect of the velocities for which the face-centre values are stored, the values prevailing at the cell face are determined by using upwind interpolation. In diffusion terms, the property gradients and the transport properties which they multiply are uniform over cell faces. The gradients are based on the supposition that the properties vary linearly, and the transport properties are arithmetic averages of those on either side of the cell faces. In source terms, the nodal values are supposed to prevail over the whole of the cell volume.

For any dependent variable the partial differential equation is finally represented by a coupled set of algebraic equations of the form

$$A_P \varphi_P = \sum_i A_i \varphi_i + S_\varphi \tag{32}$$

where the A_i's are the coefficients expressing the influence of convection and diffusion, S_φ is the integral

source term, P refers to the control volume under consideration and Σ_i indicates summation over the neighbouring nodes.

There are innumerable details in deriving the above equations which cannot be presented here because of space considerations. They all matter and should be considered as very important. For example, the discretization of the nine curvature terms, $\mathbf{V}\cdot(\rho\mathbf{V}\cdot\nabla)\mathbf{g}_n$ in equations (15), requires careful consideration to ensure automatically momentum conservation at locations of abrupt change in coordinate directions. When they are treated as source terms they lead to weak conservation, while their implicit treatment into the convection terms leads to strongly conservative formulation. A description of the treatment for these terms is given by Malin [25]. A complete description of the finite-volume equations is given in ref. [30].

2.5. *Solution procedure*

The solutions are obtained with the computer code PHOENICS [19]. The solution algorithm is based upon the iterative 'guess-and-correct' procedure of Patankar and Spalding [31], but is modified in accordance with the SIMPLEST algorithm of Spalding [32]. In general, the solution is obtained by sweeping repeatedly through the calculation domain, solving successively at each slab of cells for each dependent variable in turn. A modified version of Stone's strongly implicit method [33] is used to solve, in turn, the equations for k, ε and h. Next, the velocities are obtained by solving the momentum equations using the old iterate pressures. The solution for the velocity variables proceeds by way of the SIMPLEST procedure [32]. Then, continuity is enforced by solving a pressure-correction (p') equation [31], which determines the required adjustments to the velocities and pressures. The p'-equation is solved in a 'whole-field' manner by using a simultaneous procedure, which is also similar to Stone's method. The whole process is then repeated until the solution converges. More detailed descriptions of the solution algorithm and its features can be found in refs. [31, 32, 34].

It is worth mentioning here that the PHOENICS finite-volume equations are expressed in 'correction' form prior to their solution, thus

$$A_P\varphi'_P = \sum_i A_i\varphi'_i + R_P \tag{33}$$

where R_P is the residual defined by

$$R_P = \sum_i A_i\varphi_i^* - A_P\varphi_P^* + S_\varphi \tag{34}$$

where the φ^*'s are the in-store values of the φ's and the φ''s are the corrections which must be supplied in order to make all the equations balance. The advantages of this approach have been discussed in ref. [34].

For the present calculations on curvilinear meshes, the solution of the p'-equation proceeds without the contribution of the non-orthogonal elements of the coefficient matrix. These terms are zero for orthogonal meshes and their neglect is permissible because the terms are without influence on the final solution of the p'-equation. However, a derivation of the complete form of the p'-equation has been given by Malin [35].

Like all iterative procedures, the present solution procedure is not unconditionally stable. Convergence of the procedure is obtained through careful linearization of source terms together with appropriate relaxation of the flow variables. Two types of relaxation are employed, namely inertial and linear. Inertial relaxation may be applied to any dependent variable φ, by adding the following source term to the right-hand side of the finite-volume equation

$$S_{\varphi,I} = I(\varphi_{P,\text{old}} - \varphi_P) \tag{35}$$

where I is the so-called inertia, defined by $I = \rho V_P/T_f$ where V_P is the cell volume and T_f a false time step. In addition to the dependent variables, other quantities, such as pressure are relaxed by using conventional linear relaxation.

The convergence requirement is that for each set of finite-volume equations, the sum of the absolute residual sources over the whole solution domain be less than 1% of reference quantities based on the total inflow of the variable in question. An additional requirement is that the values of monitored dependent variables at a selected location do not change by more than 0.1% between successive iteration cycles.

2.6. *The grid and its generation*

The BFC grid used can be considered as a distorted version of the usual orthogonal grid, in which grid lines and control cells are stretched, bent and twisted in an arbitrary manner, subject to the cells retaining their topologically Cartesian character. This means that grid cells always have six sides and eight corners in the three-dimensional case.

The procedures for the generation of grid systems are of two general types: numerical solution of partial differential equations for the coordinates of the cell-corners; and construction of the coordinates by algebraic interpolation.

For Cartesian and cylindrical polar regions, a simple shearing transformation is used to generate the mesh. The method uses a linear transformation to normalize the distance between opposing physical boundaries, and uni-directional interpolation between these boundaries to generate the interior coordinates. The distribution of the coordinate points is controlled by a simple stretching function that concentrates points as required.

For the non-orthogonal regions, the elliptic grid generation approach of Warsi [36] is employed. In this approach, the Cartesian coordinates defining the grid corners in physical space are obtained as the solution of non-linear partial differential equations of the Poisson type, in which the independent variables are the computational coordinates in transformed

space. A first guess at the mesh points within the physical domain is obtained by using the algebraic technique of transfinite interpolation due to Gordon and Hall [37]. The solution of Poisson's equation proceeds by imposing Dirichlet boundary conditions on all boundaries; and the control of the coordinate lines is exercised by introducing control functions as source terms in the Poisson equations. Near-orthogonality at the boundaries is achieved by using the boundary-coordinate updating procedure described by Adamson [38]. The grid generation is performed in two dimensions, and three-dimensional problems are treated by using meshes made of stacked two-dimensional systems. This procedure is used for the present three-dimensional 'cylindrical–polar type' regions, with the two-dimensional mesh being translated and rotated to form a three-dimensional system.

3. APPLICATION OF THE MODEL

3.1. *The test case considered*

To the authors' best knowledge there is a very limited amount of experimental data that can reasonably be used to validate the present model. One such set of experiments, those referring to a Boeing-737 was used as a reference set for applying the model and judging the plausibility of its predictions. These reference predictions are presented in this section as a demonstration of the model's potential and as a motivation for further detailed experiments, that are urgently needed if these models are ever going to become real practical tools for design. Details of the Boeing-737 fuselage used and of the experimental measurements may be found in ref. [39].

3.2. *The boundary and special conditions*

The solution procedure can accommodate any type of boundary conditions. For the test case considered, in order to predict accurate results in the vicinity of the open doors, it was found desirable to extend the solution domain outside the fire compartment, into the atmosphere. At the free boundaries thus formed a uniform pressure was specified, and the atmosphere was considered at zero wind speed and ambient temperature of 25°C. At the solid boundaries the no-slip condition was used for velocities and both isothermal (at 25°C) and adiabatic conditions for temperature. The usual 'wall functions' [31] were used to compute the shear stresses and heat fluxes at the walls. The cabin fittings (e.g. seats) were modelled as blockages to flow by the use of porosities [30]. The no-slip condition was again applied for velocities, and shear stresses and heat fluxes were also computed via the 'wall functions'.

3.3. *Computational details*

All numerical calculations were performed on a NORSK 570 computer. The calculations involve large amounts of computer time on this machine. Using a grid comprising of 4200 cells (i.e. $10 \times 10 \times 42$) requires approximately 12 h of CPU while a grid of 20 328 cells (i.e. $22 \times 22 \times 42$) required in excess of 62 h of CPU. Convergence was easily obtained, using relaxation on all variables. Starting with zero initial conditions, the number of sweeps required to achieve convergence for a steady-state calculation with the $22 \times 22 \times 42$ grid was about 5000. At this stage the residuals in the balance equations had fallen to below 10^{-4} (normalized with respect to typical values of the fluxes in the field). Further sweeps of the solution domain confirmed no changes in the fields. The sum of the absolute volumetric continuity error over the whole field was insignificant, at 10^{-6}.

3.4. *Results and discussion*

The first set of results relate to the grid refinement/studies and to the comparison with the experiments. The fire consisted of a 50.7 kW heat source set in the centre of an empty B-737 fuselage. The results were found not to be particularly sensitive to the number of cells in the z-direction (along the length of the cabin). The results were however strongly dependent on the grid in the x–y plane (i.e. the cylindrical cross sections). The grids considered were $10 \times 10 \times 42$; $16 \times 16 \times 42$ and $22 \times 22 \times 42$. Of the 42 cells in the z-direction, 34 were interior cells, while four slabs of cells were used at either end outside the cabin to model realistically the domain in the vicinity of the open doors.

Figure 4(a) depicts temperature contours at the last exterior z station near the aft door, as predicted using the $22 \times 22 \times 42$ grid. Figure 4(b) shows the velocity field along the length of the fuselage. The particular plane depicted passes through the open doors and the centre of the heat source. Note the relatively cool air (at higher than ambient temperatures) entering the cabin in the bottom portion of the open doorway and the tongue of hot air billowing out from the top section of the doorway. Figure 4(b) also shows the plume above the heat source and the ceiling jets away from the plume. In this plane a two-layered structure develops in the cabin atmosphere with small re-circulation regions near the floor soffits. The neutral plane is situated midway (51%) in the open doorway.

The comparison between the numerical results and the experimental data is shown in Figs. 5(a) and (b). Figure 5(a) compares predicted temperatures with experimental data at two heights, 0.5 and 1.5 m above the cabin floor, while Fig. 5(b) is a comparison of the experimental and predicted vertical temperature stratification 6 and 13 m from the open aft door at the centreline of the fuselage.

The above results, and the many more that were obtained but not reported here due to space restrictions, indicate that there is fair overall agreement between experimental data and numerical results, for the $22 \times 22 \times 42$ grid. The coarse grids examined (comprising of about 4200 cells), while not showing good

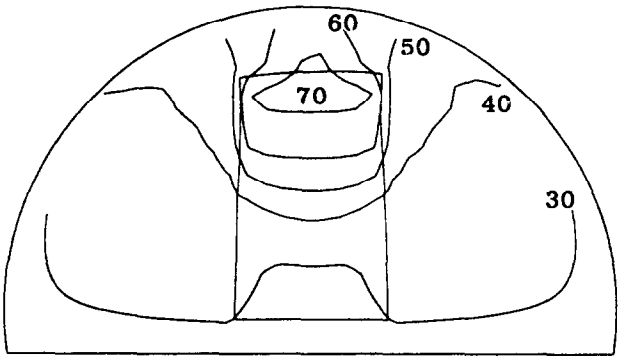

(a)

(b)

FIG. 4. (a) Temperature contours (°C) at aft doorway. (b) Velocity field along the length of the fuselage passing through the heat source (50.7 kW, 22 × 22 × 42 grid).

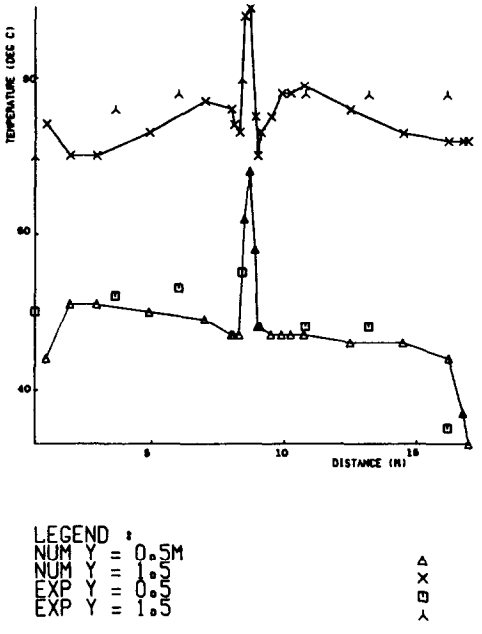

FIG. 5(a). Comparison between numerical (22 × 22 × 42 grid) and experimental [18] centreline temperatures for the 50.7 kW fire at 0.5 and 1.5 m above the floor.

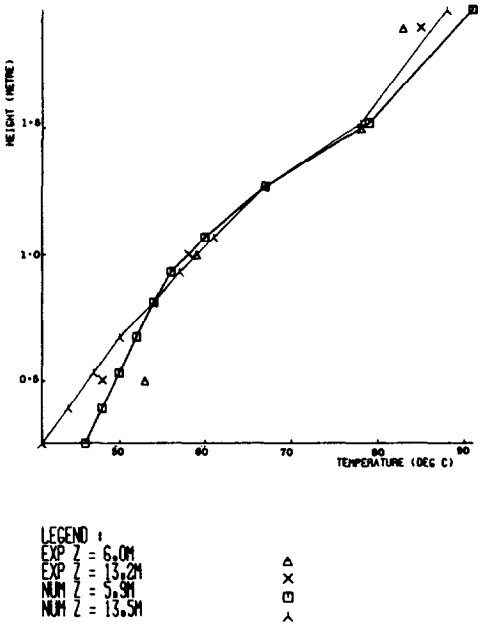

FIG. 5(b). Comparison between numerical (22 × 22 × 42 grid) and experimental [18] centreline temperature stratification at 6 and 13.2 m from the aft doorway.

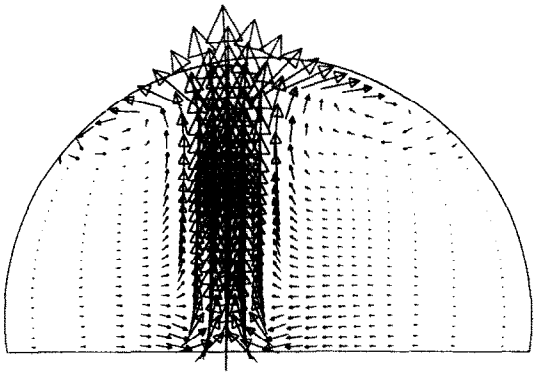

FIG. 6. Velocity field in a cylindrical section through the fire source.

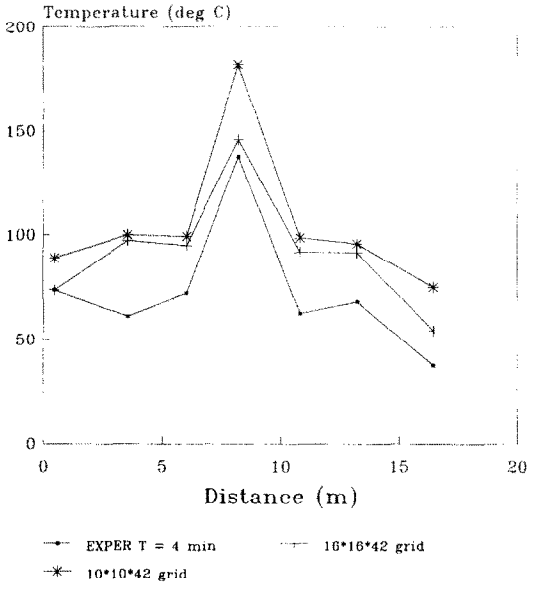

FIG. 7(a). Numerical and experimental axial temperatures for the 239 kW fire (°C) 0.5 m above the floor after 4 min.

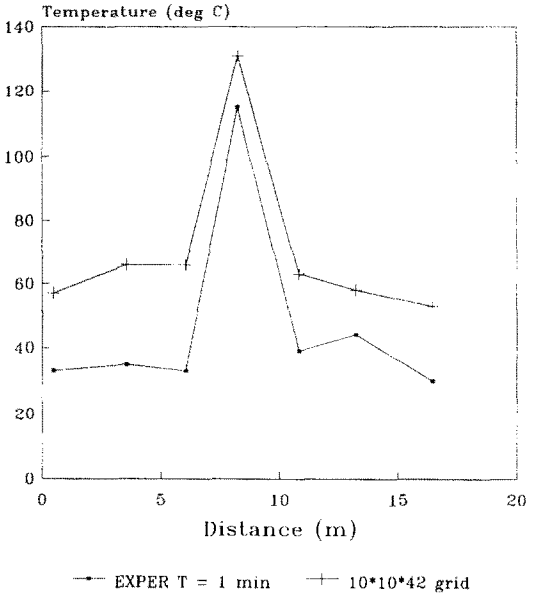

FIG. 7(b). Numerical and experimental axial temperatures for the 239 kW fire (°C) 0.5 m above the floor after 1 min.

agreement with the experiments, do still follow the broad trends found in the experimental curves. It is concluded that with a grid comprising of 20 328 cells adequate results were obtained, for the particular case considered; and that the much faster coarse-grid runs are useful when qualitative rather than quantitative results are desired. Clearly, in order to demonstrate grid independency of the results, grids much in excess of 40 000 (say $31 \times 31 \times 42$) cells must be employed.

Further study of the results reveals that the atmosphere in the cabin is stratified into horizontal layers parallel to the floor. This is in agreement with the experimental observations [39]. The air near the floor is heated to 42°C while air in the vicinity of the ceiling is heated to 88°C. Figure 6 shows the velocity field in a cylindrical section through the fire plume. Entrainment of air into the plume and impingement of the plume at the ceiling as well as the resulting re-circulation region can be seen. Temperatures within the plume are predicted to exceed 420°C. A thermocouple station was located at 0.3 m above the fuel pan. Temperatures of 300°C were recorded there, as compared with 319°C predicted by the model.

The next set of results presented concern the transient calculations, that attempt to model the first 4 min of the burn. The fire consisted of a 239 kW volumetric heat source. The grids used consisted of 4200 cells ($10 \times 10 \times 42$) and 10 752 cells ($16 \times 16 \times 42$). The preceding steady-state grid refinement studies suggest that these grids will not produce quantitatively accurate results; however these runs demonstrate the ability of the code to model the broad experimental trends in the transient mode.

Figure 7(a) compares numerical and experimental temperature data at a height of 0.5 m above the floor, for two grids ($10 \times 10 \times 42$ and $16 \times 16 \times 42$). The figure depicts temperatures along the length of the B-737 fuselage 4 min after the fire was ignited. As was observed in the steady-state case, the broad trends found in the experimental curve are followed by the numerical curves. The finer mesh while still overestimating the temperatures displays a marked improvement in predicting the maximum temperature at this height. It is expected that, as in the steady-state case, the overall accuracy of the numerical results will increase as the grid is further refined. To show the time development of temperatures, Fig. 7(b) presents the same information, for the coarse-grid run, at only 1 min after ignition.

The above comparisons between model and experimental results suggests that the model is capable of simulating non-spreading fires within aircraft fuselages. However, much more effort must be invested in the thorough validation of the code.

The remainder of this section is concerned with predicting the effect of various cabin openings, and of the cabin air-conditioning system and seating configuration on conditions within the cabin. The overall cabin dimensions and fire geometry are identical to those of the steady-state case, reported earlier.

The first set of results is concerned with investigating the effects of cabin openings and compartmentation on the temperature distribution within the aircraft cabin. Three cases are considered. In the first case both forward and aft doors are open, while in the second, the forward door is closed. The third case is similar to the first, except that the cabin contains an internal bulkhead with an open doorway. The bulkhead is located in the aft section of the cabin 1.5 m from the heat source. The doorway has identical dimensions to, and is positioned in the same location on the bulkhead as, the external door. In all three cases a grid of 8704 ($16 \times 16 \times 34$) internal cells were used. As in the earlier studies, in order to find physically realistic behaviour in the vicinity of open doors it is necessary to extend the solution domain to regions outside the fire compartment. Four slabs of cells outside each open door were used for this purpose.

Figures 8(a) and (b) show temperatures along the length of the fuselage at 0.53 m (Fig. 8(a)) and 1.49 m (Fig. 8(b)) above the floor for the first two cases investigated. As expected lower temperatures result when both forward and aft doors are open while higher temperatures occur when the forward door is closed.

Since the combustion process is not modelled, the oxygen supply has no effect on the power output of the fire, which is represented by a simple heat source. The fire is strictly non-spreading. In planned extensions to the existing model, a kinetically controlled combustion model will be provided, in which case the supply of fuel and oxidant will determine the power output of the fire. With cabin openings, the heat source behaves as if it were a pump, sucking air at ambient temperatures into the cabin, while pumping hot air out through the action of ceiling jets. With the forward door closed, temperatures in the lower regions increase by an average of 50% while temperatures in the upper regions increase by 30%. The effect of the closed forward door is felt throughout the cabin. The temperature increase within each level is almost uniform throughout the cabin, with the only exception found at the lower regions in the immediate vicinity of the open aft door. There, the inflow of air at ambient temperatures dilutes the hot compartment air.

Figure 9 shows temperatures along the length of the fuselage at 0.53 and 1.49 m above the floor for the sectioned and unsectioned cabins. Figure 9 indicates that the cabin partition offers some degree of protection from high temperatures in the aft section. In the protected cabin, temperatures in the aft section are on average 15% lower than the temperature in the unprotected cabin. Conversely, temperatures on the

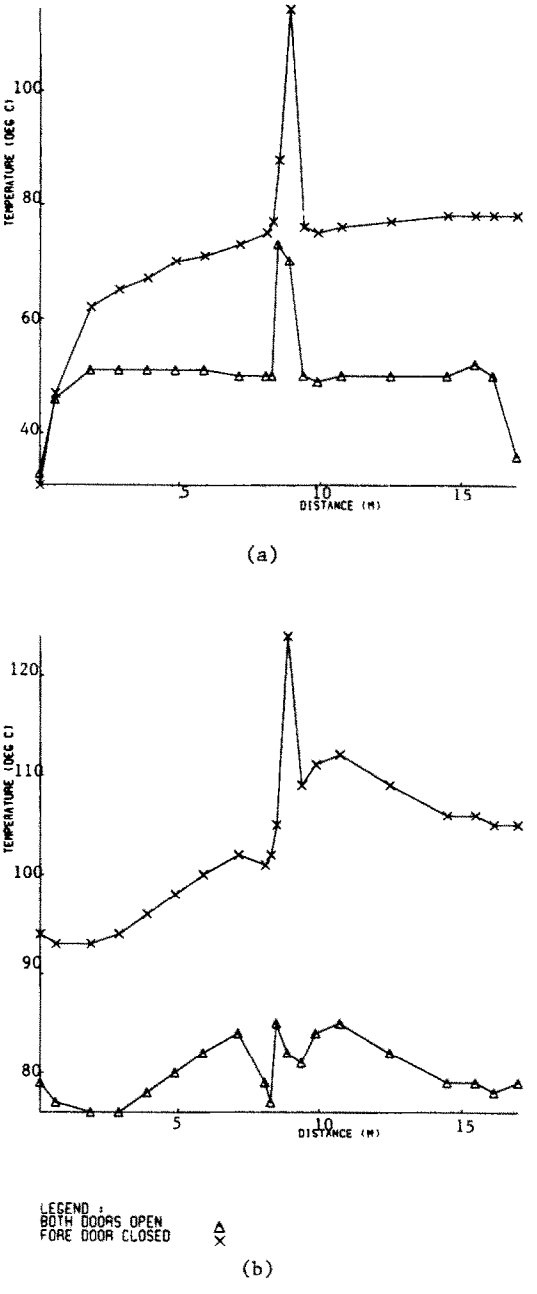

FIG. 8. Numerical centreline temperatures along the length of the cabin, at (a) 0.53 m and (b) 1.49 m above the floor, for the cases, both cabin doors open and forward cabin door closed.

fire side of the cabin are somewhat higher in the partitioned cabin, compared with temperatures in the unpartitioned cabin. In the partitioned cabin, the ceiling soffit acts to intercept the hot ceiling jet. Some of the hot gases are diverted under the soffit, while immediately behind on the fire side of the cabin a small region of recirculating air develops.

These results suggest that cabin compartmentation may offer passengers some protection from the effects of elevated temperatures in the event of fire. There

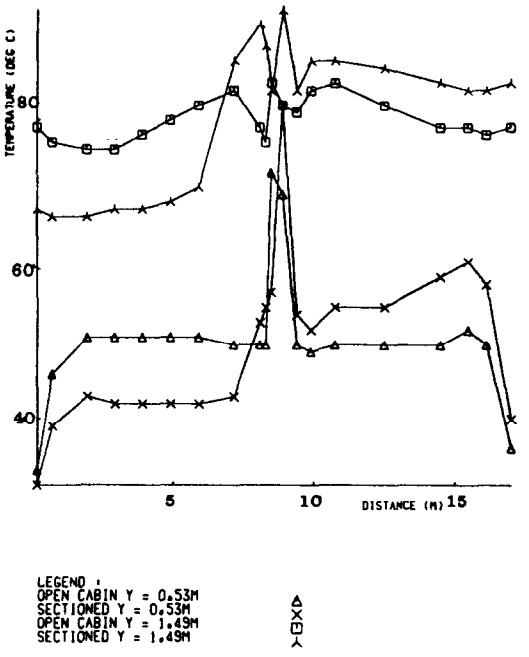

FIG. 9. Numerical temperatures (°C) along the centreline of the cabin (with partition) at 0.53 and 1.49 m above the floor.

is some experimental evidence [39] to support these claims. The earlier remarks concerning the non-spreading nature of the fire are equally valid here. The observed 'protection' offered by compartmentation assumes that the fire is not changed by the compartment configuration. In reality, the beneficial effects of the partition may be overshadowed by creating a more intense fire, thereby increasing the generation of fire hazards such as heat, smoke, toxic gas, etc. However, in the event of an external fire, these results suggest that compartmentation could lend some additional protection to passengers.

The final set of results refers to the prediction of the effect of the cabin environmental control system on the heat flow in the B-737 fuselage fitted with furniture. The fire strength was 50.7 kW. No detailed experimental results are available for comparison. The solution grid used to produce these results consists of 11 008 ($16 \times 16 \times 43$) internal cells and 1024 ($16 \times 16 \times 4$) external cells outside each open door, and is considered very coarse for the accurate prediction of the flow past the 14 rows of seats and all the other specified features.

Three venting scenarios were investigated. The first case, case A, involved no forced ventilation. In the second case, case B, fresh air is injected from the ceiling vents while hot air is sucked out from the floor vents. Case B is intended to simulate the operation of the environmental control systems found in most commercial aircraft.

Figures 10 and 11 show temperature contours and velocity vectors, respectively, in a cylindrical section located approximately midway between the fire source and the open aft doorway for the three venting scenarios. In venting cases A and C (Figs. 10(a) and (c)) the cabin atmosphere is stratified into horizontal layers parallel to the floor. Relatively cool air exists

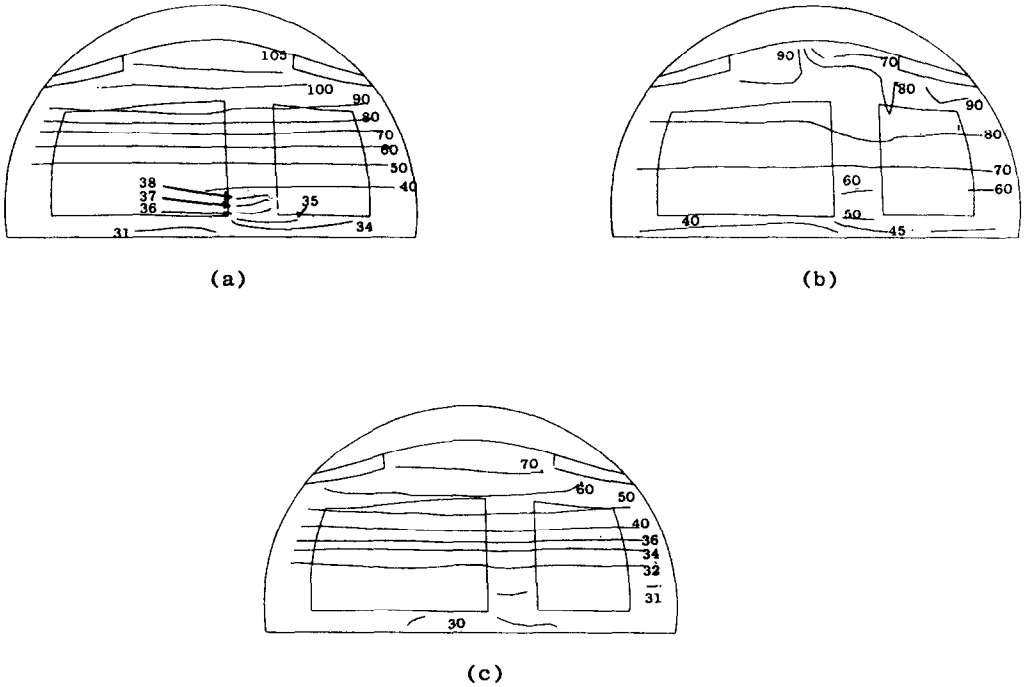

FIG. 10. Temperature contours (°C) in a cylindrical section located midway between the open aft door and the fire, for the cases, (a) no venting, (b) forward venting and (c) reverse venting.

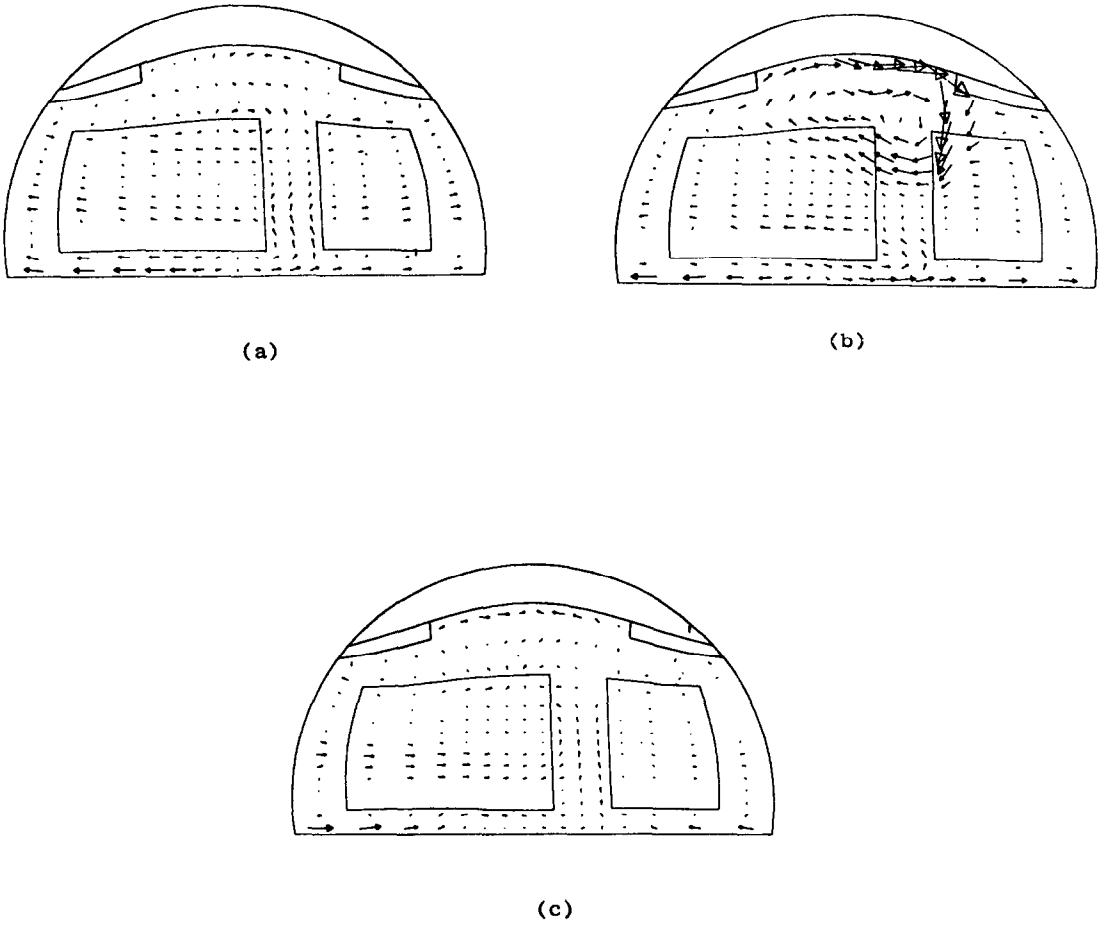

FIG. 11. Velocity vectors in a cylindrical section located midway between the open aft door and the fire, for the cases (a) no venting, (b) forward venting and (c) reverse venting. The vector scale is identical in each case.

near the floor while hotter air may be found in the vicinity of the ceiling. This is in agreement with experimental observations [40]. In venting case B (Fig. 10(b)) the atmosphere is still stratified into more or less horizontal layers near the floor; however, in the region above the seat tops this simple stratification is destroyed. The jet of cold air into the hot atmosphere sets up a large circulation region (Fig. 11(b)) throughout the length of the cabin, which extends from the ceiling to just below the seat tops. In cases A and C the tendency is for the air to rise from the floor to the ceiling region (Figs. 11(a) and (c)). The expulsion of gases from the floor vents (case B) attempts to reverse the natural tendency of hot air to rise. In venting case A (no venting) temperatures near the seat bases are approximately 40°C (Fig. 11(a)). In the case of forward venting (case B) these temperatures are increased to approximately 60°C (Fig. 11(b)) while in the reverse venting situation (case C) the temperatures are reduced to approximately 31°C (Fig. 11(c)). Temperatures near the ceiling are reduced from 105°C in venting case A (Fig. 8(a)) to 70°C in venting case C (Fig. 11(c)).

Figures 12(a)–(c) show temperature contours along the length of the fuselage, passing through the fire source and seat rows. In venting case A, temperatures of 100°C occur just above the seat tops and temperatures of 40°C occur just above the seat bases (Fig. 12(a)). In the forward venting configuration (case B) temperatures in the vicinity of the seat tops have reduced slightly to 90°C, but temperatures just above the seat bases have increased to 60°C (Fig. 12(b)). In the reverse venting situation (case C) temperatures near the seat tops and seat bases are significantly lower. In the vicinity of the seat tops the temperature has fallen to 60°C while just above the seat base the temperature is near ambient (Fig. 12(c)).

It is recognized that in view of the fact that the model has not been thoroughly validated by experiment as yet, and due to the coarseness of the grids used, these results should be viewed with some degree of reservation. However, the usefulness of reverse venting in reducing temperatures and smoke concentrations near the floor in similar fire scenarios has been observed in full scale experimental room fires [41].

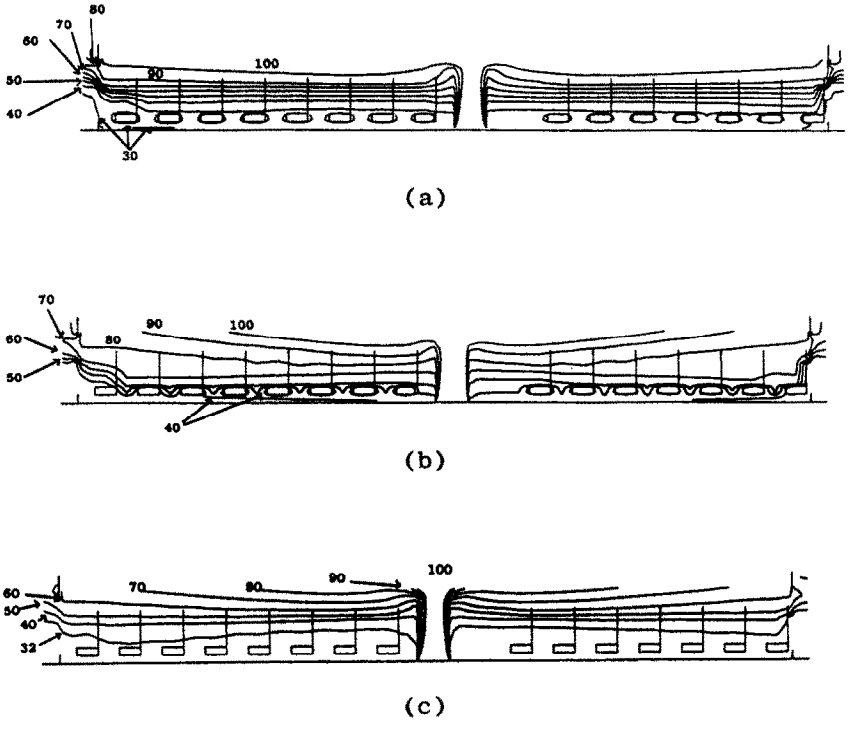

FIG. 12. Temperature contours (C) along the length of the fuselage passing through the fire for the cases, (a) no venting, (b) forward venting and (c) reverse venting.

4. CONCLUSIONS

The objective of this work is to establish a method of fire prediction which will eventually replace reliance on empiricism. It was shown that the model possesses both the flexibility and to a considerable extent the physics for such an application. However, a great amount of validation work is necessary before all the limitations are revealed and removed. Such thorough validation work is not possible at present due to the lack of extensive and meaningful experiments, that should be conducted immediately. The model was therefore applied only to one test case, that of a non-spreading fire in an aircraft cabin, for which reliable data exist. Its performance for that case, despite the turbulence modelling uncertainties and the relatively coarse grids used, proved reasonably successful. Thus, although meshes consisting of in excess of 20 000 cells are required for quantitatively accurate results, yet as little as 4200 cells produced results in qualitative agreement with experiments. Furthermore, the use of BFCs has enabled realistically shaped aircraft fuselages to be modelled for the first time.

The results indicate that openings in the aircraft fuselage have a marked effect on the temperature distribution within the cabin. With the forward bulkhead door closed while the aft door remains open, temperatures at head height reach 100°C compared to temperatures of about 60°C in the case when both doors are open. Closing the forward door has an appreciable effect throughout the cabin, even in the aft section of the fuselage. The threat to human life escalates in a corresponding manner.

In scenarios where the fire is not affected by the compartment configuration, compartmentation was observed to provide some passenger protection from the hazard of elevated temperature.

The action of the aircraft's ventilation system was observed to have a major effect on the temperature distribution within the burning fuselage. With the system extracting hot air from the floor vents and injecting cold air from the ceiling vents, as is found in most commercial passenger aircraft, temperatures in the vicinity of the seat bases increase by about 20°C over the temperatures found in the non-venting case. In the reverse flow situation temperatures fall to just above the ambient temperature.

High up in the cabin, in the vicinity of the ceiling, temperatures are also greatly reduced in the reverse venting situation.

The use of this venting strategy could lead to the control of the rate of spread of fire within the cabin. Such control is particularly pertinent to the in-flight fire scenario. The value of the method as a potential design tool lies in the fact that it can predict the *relative* changes in the field that take place as a result of a design change, even though entirely accurate results may not be obtained (because, for example, grid effects and physical modelling uncertainties such as turbulence). Furthermore, once fully validated, the

method can be applied with confidence to radically different configurations, since it is not empirical.

The method needs, of course, further development and current research is directed towards the inclusion of combustion and radiation models. Post-crash fires, in which the heat source is initially external to the cabin are also being investigated. The greatest urgency is, however, for the commissioning of detailed physical experiments in parallel with the numerical experiments.

Acknowledgements—The authors would like to thank Mr Geoff Cox (Fire Research Station) and Mr Trevor Gilpin (Civil Aviation Authority) for many useful discussions. The authors are also indebted to the SERC and the CAA for funding this research and to CHAM for allowing the use of PHOENICS.

REFERENCES

1. J. M. Ramsden, Burning questions, *Flight Int.* 121 (June 1987).
2. J. M. Ramsden, The survivable aircraft fire, *Flight Int.* 432 (August 1983).
3. E. R. Galea and N. C. Markatos, A review of mathematical modelling of aircraft cabin fires, *Appl. Math. Modell.* **11,** 162–176 (1987).
4. E. R. Galea, On the field modelling approach to the simulation of enclosure fires, *J. Fire Protection Engng* **1**(1), 11–22 (1989).
5. C. D. MacArthur, *Dayton Aircraft Cabin Fire Model*, Version 3, Vol. 1, *Physical Description*, DOT/FAA/CT-81/69-I (1981).
6. S. Kumar and G. Cox, Mathematical modelling of fires in road tunnels, 5th Int. Conf. on the Aerodynamics and Ventilation of Vech. Tunnels, Lille, p. 61 (1985).
7. N. C. Markatos, M. R. Malin and G. Cox, Mathematical modelling of buoyancy induced smoke in enclosures, *Int. J. Heat Mass Transfer* **25,** 63–75 (1982).
8. G. Cox and S. Kumar, The mathematical modelling of fire in forced ventilated enclosures, *Proc. 18th DEO Nucl. Airborne Waste Management and Air Cleaning Conf.*, U.S. Dept. of Energy, Conf., 840806, p. 629 (1985).
9. S. Kumar, N. Hoffmann and G. Cox, Some validation of JASMINE for fires in hospital wards. In *Numerical Simulation of Fluid Flow and Heat/Mass Transfer Processes* (Edited by N. C. Markatos, D. G. Tatchell, M. Cross and N. Rhodes). Springer, Berlin (1986).
10. N. C. Markatos and G. Cox, Hydrodynamics and heat transfer in enclosures, *PhysicoChem. Hydrodyn.* **5**(1), 53–66 (1984).
11. K. A. Pericleous, D. R. E. Worthington and G. Cox, The field modelling of fire in an air supported structure, paper presented at the 2nd Int. Symp. on Fire Safety Science, Tokyo, Japan (June 1988).
12. R. Huktanen, Numerical fire modelling of a turbine hall of a power plant, paper presented at the 2nd Int. Symp. on Fire Safety Science, Tokyo, Japan (June 1988).
13. K. T. Yang, J. R. Lloyd, A. M. Kanury and H. K. Sato, Numerical calculations of turbulent buoyant flow in aircraft cabins, DOT/FAA/CT-82/61 (1982).
14. K. Satoh and T. Kurvishi, Three-dimensional numerical simulations of fires in aircraft passenger compartments, 24th JAP Aviation Symp., 2C-8, pp. 1–4 (1986).
15. E. R. Galea and N. C. Markatos, Prediction of fire development in aircraft, paper presented at the 2nd Int. PHOENICS User Conf., Heathrow, London (November 1987).
16. E. R. Galea and N. C. Markatos, Modelling of aircraft cabin fires, *Fire Safety Science, Proc. 2nd Int. Symp.*, Tokyo, June 1988 (Edited by W. Takao), pp. 801–812. Hemisphere, Washington, DC (1989).
17. E. R. Galea and N. C. Markatos, Aircraft cabin fires: a numerical simulation, *Proc. 12th IMACS World Cong. on Scientific Computing*, Paris (July 1988).
18. J. F. Kuminecz and R. W. Brickner, Full-scale flammability data for validation of aircraft fire mathematical models, NASA Tech. Mem. 58244 (1982).
19. D. B. Spalding, A general-purpose computer program for multi-dimensional one- and two-phase flow. In *Mathematics and Computers in Simulations*, Prepr. 81-6, Vol. XXIII, pp. 267–276. North-Holland, Amsterdam (1981).
20. N. C. Markatos, Transport phenomena across wavy interfaces, Ph.D. Thesis, University of London (1974).
21. I. Demirdzic, A. D. Gosman, R. I. Issa and M. Peric, A calculation procedure for turbulent flow in complex geometries, *Comput. Fluids* **15**(3), 251–273 (1987).
22. N. C. Markatos, Heat, mass and momentum transfer across a wavy boundary, *Comp. Meth. Appl. Mech. Engng* **14,** 323–376 (1978).
23. B. W. Swanson, Solutions of the three-dimensional Navier–Stokes equations in non-orthogonal coordinates to calculate the flow in a log spiral impeller, ASME Paper 82-GT-268 (1982).
24. A. D. Demirdzic, A. D. Gosman and R. I. Issa, Suitability of some general coordinate versions of the fluid transport equations for numerical solution, Imperial College, Mech. Engng Dept, Fluids Section Report FS/86 (1986).
25. M. R. Malin, The prediction of interaction between gaseous jets in a rocket combustion chamber: a code evaluation study, CHAM 6690/1, London (January 1988).
26. S. Parameswaran, Finite volume equations for fluid flow based on non-orthogonal velocity projections, Ph.D. Thesis, University of London (1985).
27. M. S. Hossain and W. Rodi, Influence of buoyancy on the turbulence intensities in horizontal and vertical jets. In *Heat Transfer and Turbulent Buoyant Convection* (Edited by D. B. Spalding and N. Afgan), Vol. 2, pp. 39–51. Hemisphere, Washington, DC (1976).
28. W. Rodi, Turbulent models and their application in hydraulics—a state of the art review, SFB 80/T/127, University of Karlsruhe (1978).
29. N. C. Markatos and K. A. Pericleous, Laminar and turbulent natural convection in an enclosed cavity, *Int. J. Heat Mass Transfer* **27,** 755–772 (1984).
30. H. I. Rosten and D. B. Spalding, The PHOENICS equations, CHAM TR/99, CHAM Ltd, London (1987).
31. S. V. Patankar and D. B. Spalding, A calculation procedure for heat, mass and momentum transfer in three-dimensional parabolic flows, *Int. J. Heat Mass Transfer* **15,** 1787–1806 (1972).
32. D. B. Spalding, Four lectures on the PHOENICS computer code, CFD/82/5, CFDU, Imperial College, University of London (1982).
33. H. L. Stone, Iterative solution of implicit approximation of multi-dimensional partial differential equations, *SIAM J. Numer. Analysis* **5,** 530 (1968).
34. H. I. Rosten and D. B. Spalding, The PHOENICS reference manual for Version 1.4, CHAM TR/200, CHAM Ltd, London (1987).
35. M. R. Malin, Derivation of the pressure-correction equation for body-fitted coordinates, CHAM Development Report, CHAM Ltd, London (1983).
36. Z. U. A. Warsi, The generation of three-dimensional grids through elliptic differential systems, VKI Lecture Series 1984, Belgium (1984).
37. W. J. Gordon and C. A. Hall, Construction of curvilinear coordinate systems and applications to mesh generation, *Int. J. Numer. Meth. Engng* **7,** 461–477 (1973).

38. J. Adamson, General method of producing a boundary-fitted orthogonal curvilinear mesh, *Appl. Math. Modelling* **8**, 231–237 (1984).
39. R. Hill, P. N. Boris and G. R. Johnson, Aircraft cabin compartmentation concepts for improving post-crash fire safety, FAA-RD-76-131 (1976).
40. C. P. Sarkos, R. G. Hill and W. P. Howell, The development and applications of a full-scale wide body test article to study the behaviour of interior materials during a post-crash fuel fire, *J. Fire Flammability* **13**, 1972 (1982).
41. O. Meland, The influence of the ventilation system upon smoke-filled enclosures and the detection of smoke. In *New Technology to Reduce Fire Losses and Costs* (Edited by S. J. Grayson and D. A. Smith), p. 316. Elsevier Applied Science, Amsterdam (1986).

MODELE MATHEMATIQUE ET SIMULATION DU DEVELOPPEMENT DU FEU DANS UN AVION

Résumé—On présente un modèle mathématique tridimensionnel variable ou permanent qui décrit des feux dans une cabine d'avion. Le feu est modélisé par une simple source de chaleur et la simulation peu représenter des feux qui ne s'étendent pas. Le code de calcul utilise une formulation de coordonnées adaptée (BFC) pour décrire avec précision l'intérieur de l'avion qui n'est ni cartésien ni cylindro-polaire. Le modèle est tout d'abord utilisé pour prédire des résultats expérimentaux d'une série d'essais effectués sur un fuselage de Boeing 737. On présente les résultats en régimes variable et permanent et on les discute. On étudie l'effet des ouvertures du fuselage et des cloisons entre cabines sur la distribution de température dans l'espace vide. On examine le cas où la cabine est équipée de ses sièges, des panneaux supérieurs et on considère l'effet du système de conditionnement sur la distribution de température dans le fuselage en feu. On conclut que bien que la validation ne soit pas suffisante, à cause du manque de données expérimentales, le modèle est prometteur.

MODELLIERUNG UND SIMULATION DER ENTSTEHUNG VON FEUER IN FLUGZEUGEN

Zusammenfassung—Das stationäre oder instationäre, dreidimensionale mathematische Modell von Kabinenbränden in Flugzeugen wird vorgestellt. Das Feuer wird als einfache Wärmequelle simuliert, wobei angenommen wird, daß sich das Feuer nicht ausbreitet. Das Rechenprogramm verwendet angepaßte Körperkoordinaten, um das Innere des Flugzeugs genau zu beschreiben, das weder rechteckig noch zylindrisch ist. Das Modell wird zuerst dazu verwendet die experimentellen Ergebnisse von Brandversuchen im Rumpf einer Boeing 737 nachzurechnen. Sowohl die Ergebnisse für den stationären als auch für den instationären Fall werden dargestellt und diskutiert. Danach wird der Einfluß von Öffnungen im Rumpf und von Trennwänden in der Kabine auf die Temperaturverteilung in dem leeren Flugzeug untersucht. Wenn die vordere und die hintere Tür geöffnet sind, so daß ein natürlicher Durchzug entsteht, bleiben die Temperaturen in einem erträglichen Rahmen. Bei geschlossener vorderer und offener hinterer Tür nehmen die Temperaturen in der ganzen Kabine zu, sogar im hinteren Bereich. Bei geöffneter vorderer und hinterer Tür wird die Kabine in zwei Abteile unterteilt, das vordere enthält das Feuer. Im Vergleich zum Fall ohne Trennwand liegt die Temperatur im vorderen Teil höher und im hinteren Teil niedriger. Zum Schluß wird der Einfluß der Klimaanlage des Flugzeugs bei voll ausgestatteter Kabine auf die Temperaturverteilung in dem brennenden Rumpf untersucht. Die Ergebnisse zeigen, daß sich eine Umkehrströmung einstellt (d.h. Kaltluft wird unten eingeblasen und Heißluft an der Decke abgezogen), welche die Temperaturen im Rumpf erheblich reduziert. Obwohl das Modell bisher noch nicht genügend validiert ist, da nicht genügend geeignete Versuchsergebnisse vorliegen, sind die Ergebnisse vielversprechend.

МАТЕМАТИЧЕСКАЯ МОДЕЛЬ И ЧИСЛЕННОЕ ИССЛЕДОВАНИЕ РАЗВИТИЯ ПОЖАРА В САМОЛЕТАХ

Аннотация—В работе представлена стационарная и нестационарная математическая модель, описывающая пожары в кабине самолета. Пламя моделируется простым источником тепла, причем целью является описание нераспространяющихся пожаров. Компьютерная программа, реализующая эту модель, использует для точного описания внутренней области самолета систему координат, связанную с формой этой области и отличающуюся от декартовой и полярно-цилиндрической (body-fitted coordinate—BFC). Сначала модель используется для предсказания экспериментальных результатов, полученных при проведении серии опытов с пожарами в фюзеляже Боинга-737 (без оборудования). Приводятся и обсуждаются как стационарные, так и нестационарные результаты. Затем исследуется влияние отверстий в фюзеляже и разделения кабины на отсеки на распределение температур внутри пустой кабины самолета. При открытых дверях носовой и кормовой переборок благодаря естественной конвекции температуры сохраняются на допустимом уровне. В случае закрытой передней и открытой задней двери температура возрастает по всей кабине, даже в ее кормовой части. При открытых дверях передней и задней переборок кабина разделялась на два сообщающихся отсека, причем в переднем находилось пламя. По сравнению со случаем, когда кабина не секционирована, температура в кормовом отсеке снижается, а в носовом возрастает. Исследуется влияние системы кондиционирования воздуха в самолете на распеределение температур в горящем фюзеляже в случае, когда кабина оборудована сиденьями, потолочными панелями и верхними бункерами. Результаты позволяют сделать вывод, что при наличии обратного воздушного потока (т.е., когда холодный возлух вводится через вентиляционные отверстия в полу кабины, а горячий отсасывается через отверстия в потолке) температура во всем объеме фюзеляжа значительно снижается. В заключение отмечается, что, несмотря на недостаточную достоверность, обусловленную нехваткой соответствующих экспериментальных данных, рассмотренная модель является многообещающей.